Electronic Supplementary Material (ESI) for Environmental Science: Nano.

ARTICLE

Supporting Information for

Metallic functionalization of magnetic nanoparticles enhances the selective removal of Glyphosate, AMPA, and Glufosinate from surface water

Raghav Dogra[a†], Marco Roverso [a†], Giuseppe Di Bernardo [a], Alessandra Zanut [a], Fazel A. Monikh [a,b], Silvia Pettenuzzo [a,c], Paolo Pastore [a] and Sara Bogialli [a*]

a. *Department of Chemical Sciences, University of Padova, via Marzolo 1 - 35131 Padova, Italy*

b. *Institute for Nanomaterials, Advanced Technologies and Innovation, Technical University of Liberec Bendlova 1409/7, 460 01, Liberec, Czech Republic Address here.*

c. *Center Agriculture Food Environment (C3A), University of Trento, IT38098 San Michele all'Adige, Italy*

† These authors contributed equally to this work.

* Corresponding Author: Sara Bogialli, sara.bogialli@unipd.it

Section S1: MNPs characterization

The Fourier transform infrared (FTIR) spectra were collected between 400 to 4000 cm^{-1} by a Bruker TENSOR 27 spectrometer with a resolution of 4 cm^{-1} in transmission mode with 64 scans. The samples were analysed using a uniformly dispersed self-supporting KBr pellet (1:100), made with a pressure of more than 8 tons. The preliminary evaluation of the size distribution was done by evaluating hydrodynamic size distribution using DLS measurements. The DLS Size distribution was acquired by a Malvern Zetasizer nano spectrometer. Several tests were carried out to select the suitable dispersant by measuring the zeta potential of the suspension using a DTS1060 disposable folded capillary cell. The preliminary evaluation was carried out using the optimized dispersant and nanoparticles at a concentration of 10 mg/L. The microscopic images were taken by a JEOL JEM-2100 Plus, Transmission electron microscopy (TEM) instrument (200 KeV) using a few drops of MNPs ultra-pure water suspension deposited on a carbon-coated TEM grid (mesh 400), for morphological evaluation. The size distribution of MNPs was carried out by processing the images with the dedicated software ImageJ 1.50i analyzing a minimum of 500 particles expressed as mean diameter ± standard deviation. EDX elemental analysis were performed with EDAX Element C2B silicon drift detector. A Panalytical X'Pert-3 Powder diffractometer equipped with Cu anode (operating at 40 kV and 40 mA), incident beam mirror BBHD, sample spinner and PixCel solid state detector was used to record the X-ray diffraction (XRD) data.

FTIR Characterization

Figure 2 reports the FTIR spectra of bare MNPs particles and *MNP@pDA* particles**,** showing absorption bands at 570-580 cm^{-1} which are characteristic of the Fe-O stretching of magnetite. The signal around 1640 cm^{-1} is due to water molecules coordinated to iron oxide[1]. Additionally, a band in the range of 1600-1700 cm^{-1} is ascribable to aromatic rings of PDA (1601-1608 cm^{-1}**)** (Figure 2)[2,3]**.** Signals around 1628, 1490, and 1268 cm^{-1} correspond to the amide I, amine group attached to phenyl ring via two carbons as in phenylalanine and C–N stretching bands of the PDA coating, respectively. The broadband in the 3000 to 3400 cm^{-1} region, was assigned to the stretching of the O-H of water, probably due to an incomplete drying[4,5]. In Table S1[6–9] (Supporting data) are reported the corresponding signals of the functional moieties, depicting the surface composition of the materials corresponding to MNPs, coated *MNP@pDA,* and functionalized *MNP@pDA@*M^{+} particles, respectively.

Direct identification of the metal─O bond in the functionalized materials is not possible due to the overlapping of intense and larger bands of Fe─O and polydopamine vibrational modes. Hence, to further evaluate the metal functionalization and highlight signals directly ascribable to PDA-metal bonds, the FTIR spectrum of the *MNP@pDA* was subtracted from the FTIR spectrum of corresponding MNP@pDA@M^{+} particles.

Ti(IV) was confirmed in *MNP@pDA@*Ti^{4+} (Figure 2b) by the strong vibrational band around 553 cm^{-1} followed by weak band around 593 cm^{-1} corresponding to the asymmetric and symmetric vibrational stretching of Ti─O, respectively[10]. This was further confirmed by a very strong asymmetric stretching band of Ti─O at 643 cm^{-1}. Two additional intense bands attributing to Ti─O stretching were also observed at 1048 cm^{-1} and 1132 cm^{-1}[10]. Regarding *MNP@pDA@*Zr^{4+}, Zr(IV) was assessed by vibrational bands at 468, 596 and 738 cm^{-1} which are ascribable to Zr─O stretching (Figure 2c)[11]. Similarly, copper functionalization

was identified with typical vibrational bands of Cu─O with prominent peaks at 472, 544, 590, 638, 732 and 788 cm^{-1} (Figure 2d)[12,13].

Table S1. Comparison of FTIR vibrational bands reported vs observed in nanosorbents for Ti functionalized material. Similar considerations are applicable to Zr and Cu based nanoparticles.

Attribution	**$TiOSO_4$**	**Dopamine**	**MNP@pDA**		**MNP@pDA@Ti^{4+}**
	Theoretical			**Observed**	
ν(O-H)	-	3338	3379	3385	3385
ν(N-H)	-	3247	3251	-	-
ν(CH_2) $_{asymm}$	-	2956	2962	2959	-
ν(CH_2) $_{symm}$	-	2938	2925	2924	-
ν(C=C) ring + ρ_{sciss} (H2O)	-	1616	1621	1615	1620
ν(C-N) + ν(C-C)	-	1496	1502 1408	1490 1385	1490 1400
ν(C=C) ring	-	1284	1284	1270	1294
δ(C-H) in-plane	-	1142	1139	-	-
ν3 SO_4^{2-}	1277	-		-	1204
ν3 SO_4^{2-}	1129	-		-	1130
ν3 SO_4^{2-}	1047	-		-	-
ν1 SO_4^{2-}	967	-		-	979
δ(Ti-O)	819	-		-	821
δ(C-H) out of plane	-	815		815	-
ν(Fe-O)	580			580	580

ICP-MS analysis

Synthesized materials were subjected to microwave-assisted digestion (digestion time 3 hours, pressure 500 psi, temperature 100°C, 0.5g of concentrated HNO_3 for every 15 mg of sample), before the ICP-MS analysis. The percentage weights (% w/w) for each of the ICP-MS detectable elements present in the starting reagents are reported in Table S2, for the different materials, i.e MNPs, MNP@pDA, *MNP@pDA@*Ti^{4+}, *MNP@pDA@*Cu^{2+}, *MNP@pDA@*Zr^{4+}. MNPs are slightly contaminated by Na (2.14 %w/w) and S (0.31 %w/w), putatively due to unremoved starting material. P, K and Ca are generally not present. It is also possible to confirm the effectiveness of the MNP@pDA@M^{+} metal functionalization, ranging from 0.323 % w/w in the case of Zr(IV) to 1.890 %w/w for Ti(IV).

Table S2. Percentage weights (% w/w) for each of the considered elements (Na, P, S, K, Ca, Ti, Fe, Cu, Zr) in the different synthesized material, obtained by ICP-MS.

SAMPLES	Na (%w/w)	P (%w/w)	S (%w/w)	K (%w/w)	Ca (%w/w)	Ti (%w/w)	Fe (%w/w)	Cu (%w/w)	Zr (%w/w)
MNPs	2.14	<0.1	0.31	<0.003	0.017	0.001	>>20	0.0004	0.001
MNP@pDA	0.13	<0.1	<0.20	0.016	0.017	0.001	>>20	0.0012	0.017
MNP@pDA@Ti^{4+}	0.12	<0.1	0.62	0.008	<0.010	1.890	>>20	0.0009	0.002
MNP@pDA@Cu^{2+}	0.01	<0.1	<0.20	0.009	<0.010	0.006	>>20	0.5300	0.001
MNP@pDA@Zr^{4+}	0.01	<0.1	<0.20	<0.003	<0.010	0.012	>>20	0.0034	0.323

TEM, and EDX morphological analysis

Bare MNPs were firstly characterized by SEM analysis that showed the formation of aggregates with nanometric dimensions. A deeper insight into the size distribution was not possible due to the strong intrinsic magnetism properties which greatly impinged the magnification capacity of the SEM[1], which remained even using gold plating or by diluting samples.

A better evaluation of the morphological behaviour of the particles was obtained by Transmission Electron Microscopy (TEM)[14]. The sample size distribution accuracy was guaranteed by counting at least 500 particles. Figure 3 reports the morphological characterization of the bare MNPs (Figure 3a, 3b and 3c) and *MNP@pDA* (Figure 3d, 3e and 2f). Both samples are agglomerated of various particles but with the bare MNPs visible as spherical-shaped particles with sizes ranging from 2.4-21.3 nm (Figures 2a, and 2b). Cumulative curves shown in Figure S1a-b were also calculated, displaying the particle size distribution in terms of bandwidth and height, respectively. TEM images of *MNP@pDA* (Figure 3d-f) showed aggregations hindering the possibility to distinguish whether a single bare MNPs rather than the whole aggregate is covered with the pDA organic layer. However, coated aggregates still maintain their nanometric properties as they have dimensions of some hundred nanometres. Figure 3e and 3f reveal crystalline circular-acircular and optically dense particles covered with a very thin translucent layer, indicating the presence of the amorphous organic layer. At higher magnification (Figure 3f), the translucent organic layer can be seen as no thicker than a few nanometers, explaining the coating efficiency in *MNP@pDA.* The EDX analysis of bare MNPs shows the presence of Fe, O, Na, C and Cu (Figure S2). In particular, the large signals of iron and oxygen indicate the possible existence of iron oxides as the magnetic material (see also the FTIR analysis), whereas the small Na signal probably comes from the residual initial reagent used for the synthesis. C and Cu are due to the microscopic grid used in the analysis.

a)

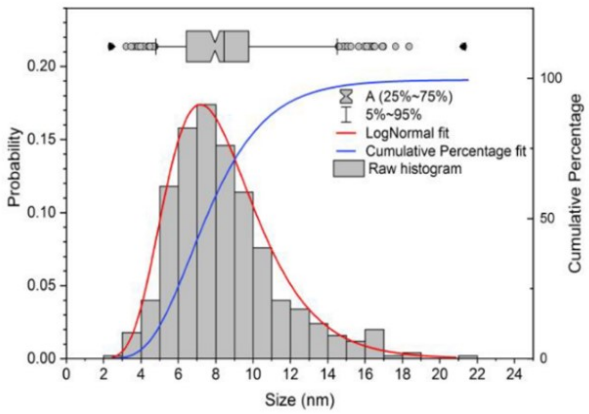

b)

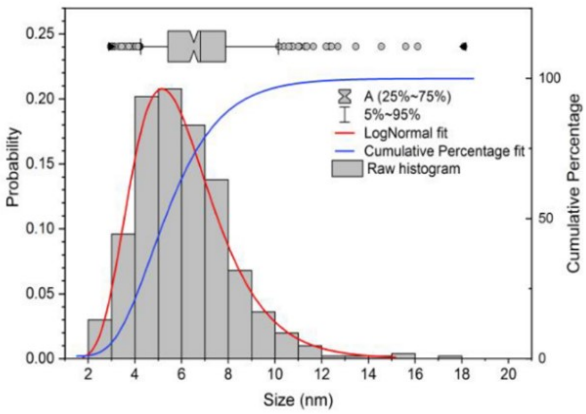

c)

Descriptive Parameters (length)	
Number of particles	500
Minimum diameter (nm)	2.4
First quartile (nm)	6.4
Median (nm)	8.0
MAD (nm)	1.7
Mean (nm)	8.4
Standard deviation (nm)	2.9
Third quartile (nm)	9.8
Maximum diameter (nm)	21.3
Mode (nm)	7.2

d)

Descriptive Parameters (width)	
Number of particles	500
Minimum diameter (nm)	2.0
First quartile (nm)	4.6
Median (nm)	5.8
MAD (nm)	1.2
Mean (nm)	6.1
Standard deviation (nm)	2.1
Third quartile (nm)	7.2
Maximum diameter (nm)	17.9
Mode (nm)	5.2

Figure S1. Size distribution of bare MNPs obtained with Transmission electron microscopy (TEM) Length (**a**) and width (**b**) are measured separately. Descriptive parameters of particles length (**c**) and width (**d**).

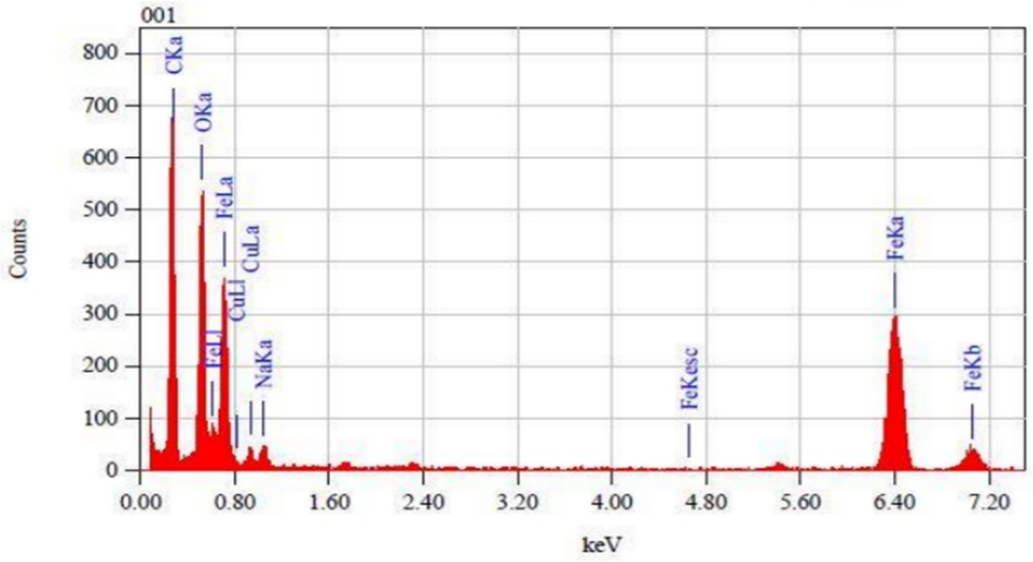

Figure S2. Energy- dispersive X-ray spectroscopy (EDX) analysis of bare magnetic nanoparticles (MNPs)

DLS measurement

DLS measurements were also done to quickly estimate the size and the size distribution of nanoparticles. Firstly, bare MNPs were analysed in ultrapure water. They showed a diameter 6-8 times larger (64-105 nm) than that obtained by TEM analysis (Figure S3a)[15]. This can be due to the presence of aggregates in bare MNPs. To decrease the effect of the intrinsic MNPs magnetic fields and optimize the results of DLS measurements, analyses were repeated by testing various sample concentrations and various aqueous solvents containing ionic modifiers such as sodium citrate, phosphate buffer saline (PBS), polyethylene glycol (PEG), and TRIS buffer to stabilize the colloidal particle dispersion in the media[1]. Optimized conditions were evaluated by considering the zeta potential of the suspension, in order to reach the range required for stable colloidal dispersion (beyond -20 to 20mV) at a constant particle Concentration of 10 mg/L. Reliable results, comparable with TEM data, were obtained by using 10 mM sodium citrate as a solvent (Figure S3b).

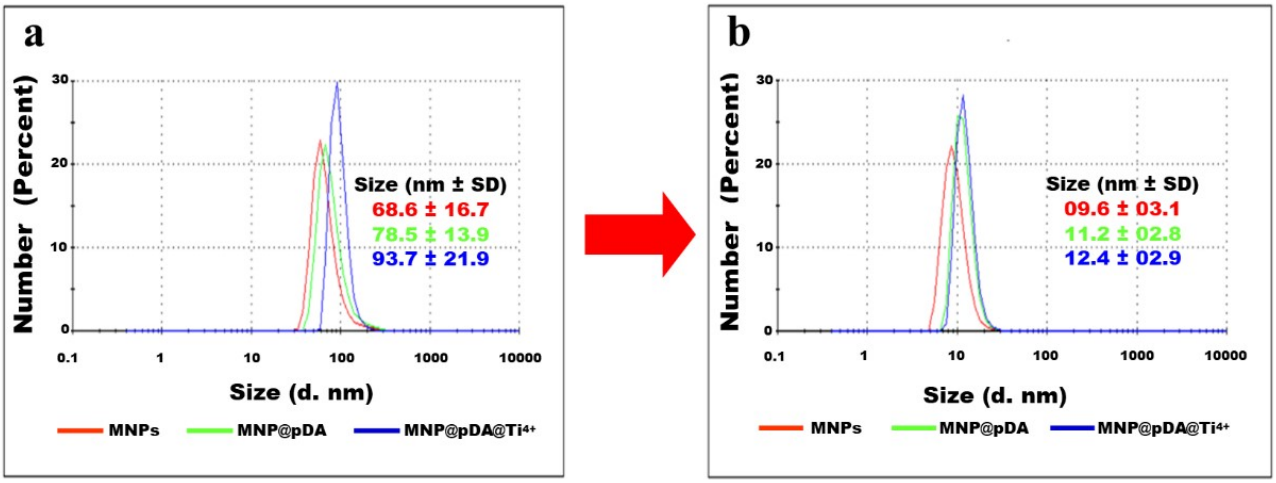

Figure S3. DLS size distribution of selected MNPs, MNP@pDA, and MNP@pDA@Ti^{4+} 10mg/L solution with a) Milli Q water b) Sodium Citrate 10mM.

XRD analysis

The XRD results (Table S3) confirm the presence of maghemite in all the samples. Magnetite has the same main peaks of maghemite, thus it is impossible to evaluate its presence when there is maghemite. The apparent mean of the crystallite size along the crystallographic direction 113 (relative to the main peak of maghemite) are derived, for each sample, by Scherrer Formula after profile fitting.

Table S3. Qualitative XRD analysis and estimate of apparent mean crystallite size relative to 113 crystallografic direction by Scherrer Formula.

Samples	Mineral name	Apparent Mean Crystallite Size (nm)
MNPs	maghemite	7.9
MNPs@pDA	maghemite	8.1
MNPs	magnetite	8.2
MNPs@PDA	maghemite	8.3
MNPs@pDA@Ti^{4+}	maghemite	8.5

Section S2: evaluation of the NSs adsorption capability

Experimental setup

A schematic illustration of the experimental set up is represented in Figure S4 to show the steps of the experiment.

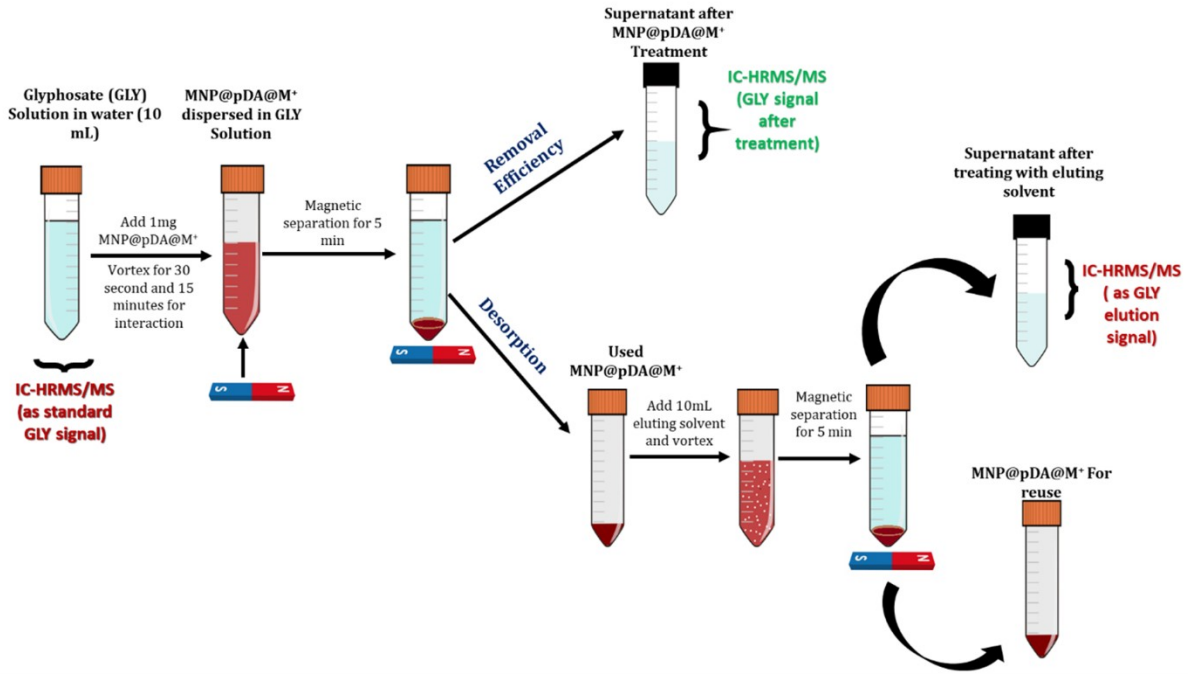

Figure S4. Schematic representation of General procedure adopted for evaluating GLY adsorption capacity of the MNP@pDA@M^+.

Quantification of GLY, AMPA and GLUF

After treating contaminated solutions, MNPs were magnetically separated from the solution at specific time intervals, and the residual was determined by ion chromatography coupled to high resolution tandem mass spectrometry (IC-HRMS/MS) using the Dionex ICS-6000 instrument (Thermofisher Scientific, Waltham, Massachusetts, USA) coupled with a Q Exactive™ hybrid quadrupole-Orbitrap™ mass spectrometer (Thermo Scientific, Waltham, Massachusetts, USA). The IC was equipped with a pumping module (ICS-6000 SP), an eluent generator via cartridge (ICS-6000 EG), a column compartment thermostat (ICS-6000 DC), an electrochemical ion suppressor (Dionex ADRS 600 2 mm), and a conductivity detector (ICS-6000 CD)[1,2]. The separation was performed by the Ion-Pac AS 19-4 µm (2 x 250mm) as analytical column and the Ion-Pac AS 19-4 µm (2 x 50mm) as precolumn. The injection volume was 25 µL and the eluent flow rate was 0.25 mL/min. The mobile phase gradient profile was as follows (t in min): $t_{0\text{-}6}$, 20 mM KOH; $t_{6\text{-}14}$, 20-55 mM KOH; $t_{14\text{-}21}$, 55 mM KOH; $t_{21\text{-}22}$, 55-20 mM KOH, $t_{22\text{-}30}$, 20 mM KOH. Acetonitrile was added post column at a flow rate of 0.15 mL/min. The MS conditions were: electrospray (ESI) ionization in negative mode, spray voltage 2.8 kV, capillary temperature 320°C, sheath gas flow rate 40 a.u., auxiliary

gas flow rate 20 a.u., auxiliary gas temperature 280°C, RF level 55. Data were acquired in Parallel Reaction Monitoring mode, by selecting the $[M-H]^-$ species for all the parents' ions and fragmentation energy reported in Table S4. The integration of the chromatographic peak of each analyte was performed by selecting the Extracted Ion Chromatogram (EIC) of the corresponding fragment ion (Section S3, Table S4) with an accuracy of 5 ppm.

Table S4. The Parallel reaction mode parameters for selecting the peaks for AMPA, GLY and GLUF

Analyte	Parent ion (*m/z*)	Fragment Ion (*m/z*)	Collision energy (NCE)
AMPA	110.0013	62.9926	50
GLY	168.0067	62.9926	50
GLUF	180.0431	94.8889	50

The influence of the GLY-MNP ratio

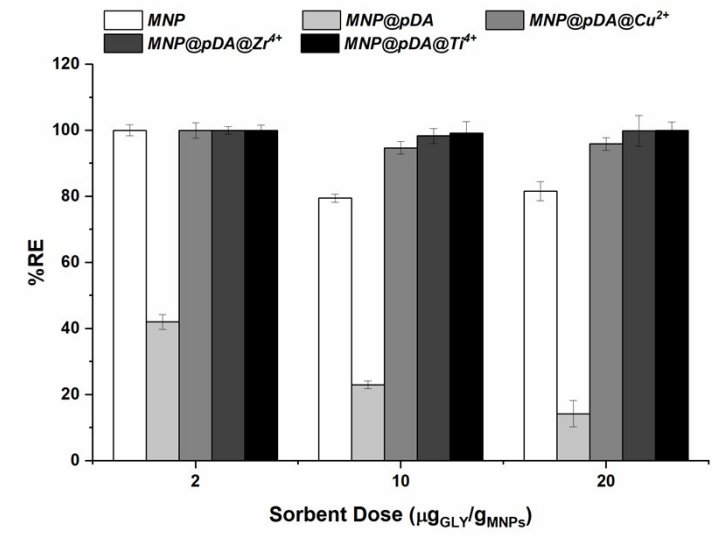

Figure S5. Effect of the GLY/MNPs ratio (sorbent dose) on GLY removal efficiency (RE%) of *MNP* (white), *MNP@pDA* (light gray), *MNP@pDA@*Cu^{2+} (gray), *MNP@pDA@*Zr^{4+} (dark gray), *MNP@pDA@*Zr^{4+} (black) at constant contact time (15 min) and room temperature. Data are reported as mean ± S.E.M. (n=3).

Section 5: Application in real water samples

Table S5. Results illustrating the complete removal of GLY below LOD from real water sample on the application of MNP@pDA@M^{4+}

Type of MNPs	Concentration of GLY (mg/L)	
	Before Treatment	**After Treatment**
MNPs@pDA@Ti^{4+}	0.17±0.02	< LOD
MNPs@pDA@Zr^{4+}	0.17±0.02	< LOD

Section 6: Testing the reusability

We measured the desorption (elution) of GLY from the MNP@pDA@M^+ after performing the removal experiment and recovering the particles using a magnet. The solvents NH_4OH and KOH were applied for the eluting the chemicals from the particles. The experiments were performed at room temperature, 500 μg analyte/gNS of GLY and contact time of 15 min. The results are presented in Figure S5. Residue post adsorption and desorption of GLY from the same batch using different solvents were presented in red and green, respectively. The pH values are reported for each test.

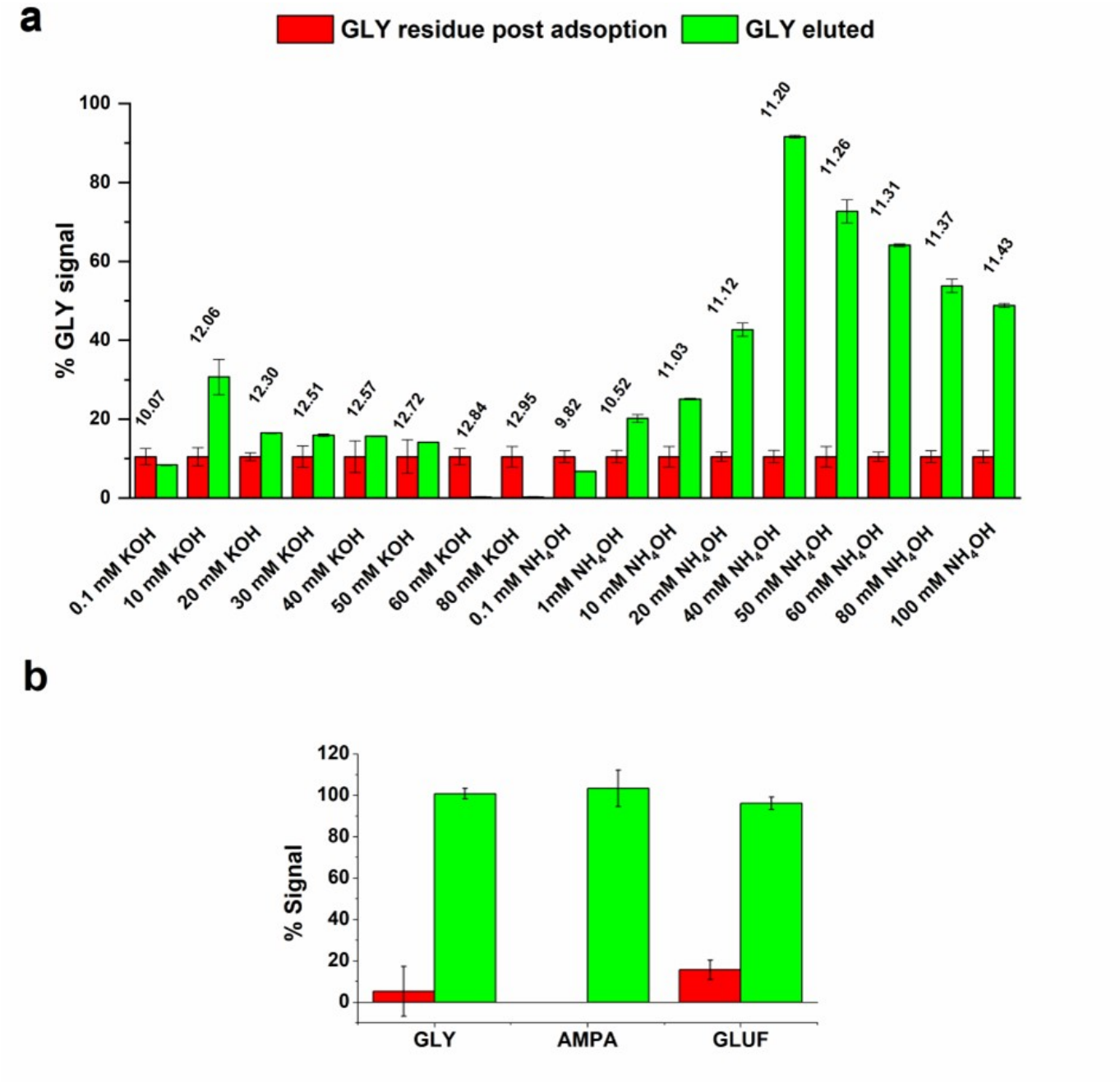

Figure S6. a) Elution capacity measurements of GLY from with MNP@pDA@Ti^{4+} using different solvents, room temperature, 500 µg analyte/gMNP of GLY and contact time of 15 min. Residue post adsorption (red) and desorption (Green) of GLY from the same batch using different solvents; pH values are reported for each test. b) Adsorption and desorption of 20 µg/L each one of GLY, AMPA and GLUF at room temperature using MNP@pDA@Ti^{4+} and 40 mM NH_4OH eluting solvents (n=3).

References

1. Lobato, N. C. C., Mansur, M. B. & De Mello Ferreira, A. Characterization and Chemical Stability of Hydrophilic and Hydrophobic Magnetic Nanoparticles. *Mater. Res.* **20**, 736–746 (2017).

2. Zhu, L. P., Jiang, J. H., Zhu, B. K. & Xu, Y. Y. Immobilization of bovine serum albumin onto porous polyethylene membranes using strongly attached polydopamine as a spacer. *Colloids Surfaces B Biointerfaces* **86**, 111–118 (2011).

3. Socas-Rodríguez, B., Hernández-Borges, J., Salazar, P., Martín, M. & Rodríguez-Delgado, M. Á. Core–shell polydopamine magnetic nanoparticles as sorbent in micro-dispersive solid-phase extraction for the determination of estrogenic compounds in water samples prior to high-performance liquid chromatography–mass spectrometry analysis. *J. Chromatogr. A* **1397**, 1–10 (2015).

4. Wang, Y. *et al.* Preparation of polydopamine coated Fe3O4 nanoparticles and their application for enrichment of polycyclic aromatic hydrocarbons from environmental water samples. *J. Chromatogr. A* **1283**, 20–26 (2013).

5. Zhu, B. & Edmondson, S. Polydopamine-melanin initiators for Surface-initiated ATRP. *Polymer (Guildf).* **52**, 2141–2149 (2011).

6. Jiang, J., Zhu, L., Zhu, L., Zhu, B. & Xu, Y. Surface characteristics of a self-polymerized dopamine coating deposited on hydrophobic polymer films. *Langmuir* **27**, 14180–14187 (2011).

7. Noda, L. K., Sensato, F. R. & Gonçalves, N. S. Titanyl sulphate, an inorganic polymer: Structural studies and vibrational assignment. *Quim. Nova* **42**, 1112–1115 (2019).

8. Zangmeister, R. A., Morris, T. A. & Tarlov, M. J. Characterization of polydopamine thin films deposited at short times by autoxidation of dopamine. *Langmuir* **29**, 8619–8628 (2013).

9. Yu, X., Fan, H., Liu, Y., Shi, Z. & Jin, Z. Characterization of carbonized polydopamine nanoparticles suggests ordered supramolecular structure of polydopamine. *Langmuir* **30**, 5497–5505 (2014).

10. Moran, P. D. *et al.* Vibrational Spectra and Molecular Association of Titanium Tetraisopropoxide. *Inorg. Chem.* **37**, 2741–2748 (1998).

11. Khomenkova, L. *et al.* Effect of Ge Content on the Formation of Ge Nanoclusters in Magnetron-Sputtered GeZrOx-Based Structures. *Nanoscale Res. Lett.* **12**, 1–12 (2017).

12. Tanvir, N. B., Yurchenko, O., Wilbertz, C. & Urban, G. Investigation of CO 2 reaction with copper oxide nanoparticles for room temperature gas sensing. *J. Mater. Chem. A* **4**, 5294–5302 (2016).

13. Vasantharaj, S. *et al.* Synthesis of ecofriendly copper oxide nanoparticles for fabrication over textile fabrics: Characterization of antibacterial activity and dye degradation potential. *J. Photochem. Photobiol. B Biol.* **191**, 143–149 (2019).

14. Xie, L., Jiang, R., Zhu, F., Liu, H. & Ouyang, G. Application of functionalized magnetic nanoparticles in sample preparation. *Anal. Bioanal. Chem. 2013 4062* **406**, 377–399 (2013).

15. Steven V. Ley, C. M. R. L. *Ultrasound in Synthesis - Steven V. Ley, Caroline M.R. Low - Google Books*. (Springer-Verlag, 11989BC).

